

Alma Mater Studiorum Università di Bologna  
Archivio istituzionale della ricerca

Fractal Neural Network: A new ensemble of fractal geometry and convolutional neural networks for the classification of histology images

This is the final peer-reviewed author's accepted manuscript (postprint) of the following publication:

*Published Version:*

Fractal Neural Network: A new ensemble of fractal geometry and convolutional neural networks for the classification of histology images / Roberto G.F.; Lumini A.; Neves L.A.; do Nascimento M.Z.. - In: EXPERT SYSTEMS WITH APPLICATIONS. - ISSN 0957-4174. - STAMPA. - 166:(2021), pp. 114103.1-114103.11. [10.1016/j.eswa.2020.114103]

*Availability:*

This version is available at: <https://hdl.handle.net/11585/784605> since: 2020-12-17

*Published:*

DOI: <http://doi.org/10.1016/j.eswa.2020.114103>

*Terms of use:*

Some rights reserved. The terms and conditions for the reuse of this version of the manuscript are specified in the publishing policy. For all terms of use and more information see the publisher's website.

This item was downloaded from IRIS Università di Bologna (<https://cris.unibo.it/>).  
When citing, please refer to the published version.

(Article begins on next page)

This is the final peer-reviewed accepted manuscript of:

Guilherme Freire Roberto, Alessandra Lumini, Leandro Alves Neves, Marcelo Zanchetta do Nascimento, Fractal Neural Network: A new ensemble of fractal geometry and convolutional neural networks for the classification of histology images, *Expert Systems with Applications*, Volume 166, 2021, 114103, ISSN 0957-4174,

The final published version is available online at:  
<https://doi.org/10.1016/j.eswa.2020.114103>

#### Terms of use:

Some rights reserved. The terms and conditions for the reuse of this version of the manuscript are specified in the publishing policy. For all terms of use and more information see the publisher's website.

*This item was downloaded from IRIS Università di Bologna (<https://cris.unibo.it/>)*

***When citing, please refer to the published version.***

# Fractal Neural Network: a new ensemble of fractal geometry and convolutional neural networks for the classification of histology images

Guilherme Freire Roberto<sup>a,\*</sup>, Alessandra Lumini<sup>b</sup>, Leandro Alves Neves<sup>c</sup>,  
Marcelo Zanchetta do Nascimento<sup>a</sup>

<sup>a</sup>*Faculty of Computation (FACOM) - Federal University of Uberlândia (UFU), Av. João Naves de Ávila 2121, BLB, 38400-902, Uberlândia, MG, Brazil*

<sup>b</sup>*Department of Computer Science and Engineering (DISI) - University of Bologna, Via dell'Università 50, 47521, Cesena, FC, Italy*

<sup>c</sup>*Department of Computer Science and Statistics (DCCE), São Paulo State University (UNESP), R. Cristóvão Colombo, 2265, 15054-000, São José do Rio Preto, SP, Brazil*

---

## Abstract

Classification of histology images is a task that has been widely explored on recent computer vision researches. The most studied approach for this task has been the application of deep learning through CNN models. However, the use of CNN in the context of histological images classification has yet some limitations such as the need of large datasets, the slow training time and the difficult to implement a generalized model able to classify different types of histology tissue. In this paper, we propose an ensemble model based on handcrafted fractal features and deep learning that consists on fusing the classification of two CNN by applying the sum rule. We apply feature extraction to obtain 300 fractal features from different histological datasets. These features are reshaped into a  $10 \times 10 \times 3$  matrix in order to compose an artificial image that is given as input to the first CNN. The second CNN receives as input the correspondent original image. After combining the results of both

---

\*Faculty of Computation (FACOM) - Federal University of Uberlândia (UFU), Av. João Naves de Ávila 2121, BLB, 38400-902, Uberlândia, MG, Brazil. Tel.: +55 34 32394470

*Email addresses:* [guilhermefroberto@gmail.com](mailto:guilhermefroberto@gmail.com) (Guilherme Freire Roberto), [alessandra.lumini@unibo.it](mailto:alessandra.lumini@unibo.it) (Alessandra Lumini), [leandro@ibilce.unesp.br](mailto:leandro@ibilce.unesp.br) (Leandro Alves Neves), [marcelo.zanchetta@gmail.com](mailto:marcelo.zanchetta@gmail.com) (Marcelo Zanchetta do Nascimento)

CNN, we were able to obtain accuracies that range from 89.66% up to 99.62% on five different datasets. Moreover, our model was able to classify images from datasets with imbalanced classes, without the need of images having the same resolution, and in a relative fast training time. We also verified that the obtained results are compatible with the most recent and relevant studies recently published in the context of histology image classification.

*Keywords:* deep learning, fractal features, classification ensemble, histology images

---

## 1. Introduction

Histopathology consists on the analysis of histological tissue and the study of how diseases affect the cells. Usually, a pathologist performs this analysis by observing histology slides through a digital microscope [7]. However, this task is prone to errors as evaluation is often subjective and dependent on the pathologist's experience, which may lead to misdiagnosis [38].

In order to provide support to pathologists, several computer vision techniques have been applied on images obtained from histology slides. These techniques consist on performing a series of evaluations on the input images and then provide a classification based on pre-defined classes, such as benign or malignant. This is a complex procedure, often referred as computer aided-diagnosis (CAD), which can be split into several stages, from image acquisition, going through pre-processing, segmentation, feature extraction, feature selection and classification [27]. Therefore, a CAD system is an important tool that provides a second view to the pathologist, increasing the diagnosis accuracy and reducing the amount of time and physicians required to label large amounts of medical exams [18]. In this paper, we focus on the feature extraction and classification stages of a CAD system for histological image analysis.

Different techniques can be applied to extract handcrafted features from these images. Among the most recently researched techniques, we can cite local binary pattern (LBP), gray level co-occurrence matrix (GLCM), speeded up robust features (SURF) or fractal geometry, which were applied for kidney tissue analysis [53], breast cancer classification [64], colon cell nuclei detection [2] and lymphoma classification [47], respectively. However, the main research focus for this area in recent years has been the application of

27 deep learning approaches, more specifically, the use of convolutional neural  
28 networks (CNN).

29 CNN have shown to be efficient for the classification of objects, mainly  
30 in multiclass problems [28, 24]. However, these relevant results are not as  
31 often in the context of histological images [10, 59, 4]. One of the reasons  
32 is that CNN require large sets for training, given that a major part of the  
33 public histological datasets available contain a limited number of samples  
34 [63]. To handle this situation, more data is generated for training by applying  
35 rotation, mirroring or region cutting on the images. Nonetheless, this data  
36 augmentation raises even more the high computational cost of CNN [32].

37 One of the possible solutions to reduce processing time consists in simpli-  
38 fying the network architecture by reducing the amount of layers. However,  
39 the removal of deeper layers may hinder the image analysis from a global  
40 perspective [4], which may compromise the network performance. Some al-  
41 ternative approaches, like hybrid networks, have been explored. These ap-  
42 proaches associate non-deep learning techniques such as Gabor filters or LBP  
43 operators with the convolution operations of CNN, which allows to replace  
44 some of the network’s layers [28, 24]. Other approaches aim to achieve a  
45 lower processing time by reducing the images’ dimensionality. In [29], the  
46 authors applied Haar-wavelet decomposition on breast histology images and  
47 used the decomposed images as input to a CNN.

48 Recent researches have shown that a fusion of handcrafted features with  
49 deep learning models can enhance common approaches [40]. The application  
50 of fractal features, which have provided relevant results in the context of  
51 histological images classification [46, 48], could also be associated to hybrid  
52 CNN. In [62], CNN were applied to extract values from an invariant fractal  
53 dimension filter for detecting object curves in grayscale images. The authors  
54 in [37] applied multifractal analysis to quantify and detect breast cancer,  
55 classifying the generated feature vectors using deep learning. However, an  
56 approach similar to the proposed by [29], wherein the CNN receives as input  
57 secondary images generated by a specific technique has not yet been exper-  
58 imented in the fractal geometry context. Moreover, methods that directly  
59 associate fractal geometry with CNN through an ensemble for the classifica-  
60 tion of histological images were not found in the literature.

61 In this paper, we propose a novel approach, which we name as Fractal  
62 Neural Network (FNN), to classify histological images through the associ-  
63 ation of fractal geometry and CNN. In our proposal, fractal features are  
64 extracted from the histology images and then rearranged in order to gen-

65 erate an artificial RGB feature image. Both this artificial image and the  
66 correspondent original image are given as input to a CNN ensemble, wherein  
67 a classification based on the sum rule outputs the class prediction. This new  
68 method provides the following contributions to the literature:

- 69 1. double-CNN classification ensemble wherein an image generated from  
70 handcrafted fractal features and the respective regular image are given  
71 as input to a CNN;
- 72 2. An adaptive method that is able to classify different sets of histological  
73 images, including datasets with imbalanced classes, few samples and  
74 varying image dimensions;
- 75 3. The combination of different fractal measures to provide a set of fea-  
76 tures capable of describing the image’s properties;
- 77 4. A deep learning model that requires a small number of training epochs,  
78 even when classifying new types of histology images.

79 In the second section of this paper, recent researches regarding the clas-  
80 sification of histological images are discussed. In Section 3, we provide a  
81 technical background on the use of fractal geometry for feature extraction of  
82 color images. The proposed methodology is presented on Section 4, and in  
83 Section 5, the results obtained by applying the method on the tested datasets  
84 are presented and discussed. Finally, we conclude the paper at Section 6, with  
85 an overview of the obtained results and suggestions for future researches.

## 86 **2. Related Work**

87 Plenty of advances have been achieved by researchers on the field of medi-  
88 cal image classification recently, wherein deep learning approaches have been  
89 playing a major role on such improvements mainly on the feature extraction  
90 and classification stages of a CAD system.

### 91 *2.1. Breast Tumors Classification*

92 Breast cancer is a disease that initially starts with a tumor in the breast  
93 area but can later grow to surrounding tissues. This is the most common  
94 cancer type among women, although it also affects men. According to the  
95 Nacional Cancer Institute, 276,480 new cases and 42,170 deaths are expected  
96 in the United States for 2020 [17]. Due to high incidence, breast cancer  
97 detection became an important focus on computer vision research.

98 In [13], an artificial neural network composed by two modules was built  
99 to classify 58,000 patches with dimensions  $15 \times 15$  of benign and malignant  
100 breast tumors. The first module performs an unsupervised feature extraction  
101 based on stacked denoising auto encoder. The second part, consists of a soft-  
102 max classifier. This approach was able to provide accuracies of 98.27% and  
103 90.54% for the detection of benign and malignant tumors, respectively. Mul-  
104 tiple instance classification have also recently provided relevant results for the  
105 classification of breast tumors. Using a spatial decomposition technique that  
106 produces spatial and color components corresponding to 2nd and 3rd dimen-  
107 sion of data tensors related to the input images, the authors in [44] were able  
108 to achieve an accuracy of 84.67% using a multiple instance classifier. Their  
109 method performed faster than other common approaches and could also ob-  
110 tain an accuracy of 79.33% even with 90% of missing data. Handcrafted  
111 image features have also been used as complementary to deep learning ap-  
112 proaches. In [64], nuclei segmentation of breast tumors is performed through  
113 the application of a CNN. Then, texture features obtained from different  
114 handcrafted approaches are extracted from the segmented images and given  
115 as input to an SVM classifier. After applying the Relief feature selection  
116 method, the method was able to obtain an accuracy of 96.7%. In [31], the  
117 authors used data-augmentation to significantly increase the number of sam-  
118 ples of the breast cancer dataset by generating  $112 \times 112$  sized patches. To  
119 improve classification, the authors applied a simple six-layer CNN to remove  
120 mislabeled patches. After associating multiscale feature extraction with a  
121 CNN classifier, an accuracy of 100% was obtained.

## 122 *2.2. Colorectal Tumors Classification*

123 Colorectal cancer consists on the growth of malignant polyps in the colon  
124 or rectum area. This is the fourth most common type of cancer, with 147,950  
125 new cases and 53,200 deaths expected for 2020 in the United States [17].  
126 Several researches have been published in recent years aiming to improve the  
127 automated diagnosis of this type of cancer.

128 In [11], the authors used a 31-layers CNN to perform the classification of  
129 colorectal histological images, achieving accuracies of 93.24% and 96.97% for  
130 5-class and 2-class classification respectively. Similar results were obtained in  
131 [51] when classifying 4 categories of colorectal tumors with a smaller network  
132 (12 layers), wherein an accuracy of 93.28% was obtained after 400 epochs of  
133 training. Furthermore, some researchers have been recently exploring ap-  
134 proaches that consist of ensembles of different CNN models. The authors of

135 [5], for instance, first applied color normalization on the images of the col-  
136 orectal dataset. Then, the normalized images were given as input to an U-  
137 Net CNN in order to perform segmentation, aiming to remove non-glandular  
138 areas. A different CNN model (GoogLeNet) was used to classify the seg-  
139 mented images. This approach provided an accuracy of 85%. An ensemble  
140 of different CNN was also published by [57] for the detection of colorectal  
141 tumors. The authors developed an approach based on generative adversarial  
142 networks (GAN) wherein the generator was implemented as an U-Net and  
143 the discriminator is a standard CNN. With 3,000 patches of colorectal tumor  
144 images available, the method provided an F-score of 0.940. According to the  
145 authors, this approach deals well with class imbalance, due to its capacity  
146 to retrain the network when new classes are added using the CNN Inception  
147 v3.

### 148 *2.3. Non-Hodgkin Lymphomas Classification*

149 Lymphomas are a type of cancer that affects cells of the immunological  
150 system, wherein the most common occurrence is the non-Hodgkin lymphoma  
151 (NHL). According to statistics, 77,240 new cases and 19,940 deaths caused  
152 by NHL are expected for 2020 in the United States [17]. Although it accounts  
153 for only 3.3% of all cancer-related deaths, NHL are divided into categories,  
154 each one requiring specific treatments. Therefore, computer methods that  
155 are able to identify the NHL type are an important tool to provide support  
156 to pathologists [43].

157 In [22], NHL images were split into several  $36 \times 36$  patches which were  
158 later cropped to  $32 \times 32$  sub-patches using the Caffe framework, generating  
159 825,000 training patches. These patches were given as input to a standard  
160 AlexNet architecture and an accuracy of 96.58% was achieved with the use  
161 of a voting scheme for classification. However, the use of deep learning tech-  
162 niques is not mandatory to obtain relevant results for such task, as shown by  
163 [25]. On this approach, the images were firstly converted into grayscale and  
164 then, 130 non-overlapped patches with size  $100 \times 100$  were extracted from  
165 each image, resulting in a total of 48,620 patches. An unsupervised feature  
166 extraction method was applied along with ordinary texture approaches to  
167 extract 680 handcrafted features. These features were classified using a hi-  
168 erarchical 2-stages machine learning method, which resulted in an accuracy  
169 of 97.96%. In [6], the authors proposed a method that applies both deep  
170 learning and handcrafted features for NHL classification. On this approach,  
171 color, statistical and texture features were extracted from patches cropped



172 out of the original images and given as input at a random forest classifier.  
173 These patches were also used to feed a GoogLeNet CNN. Both the random  
174 forest and the CNN provided patch predictions which were processed using  
175 weighted sum to generate a final classification prediction. The obtained ac-  
176 curacy was of 99.10%. Fractal features have also provided relevant results  
177 on NHL classification recently. In [36], fractal geometry was used to ex-  
178 tract multiscale and multidimensional features from RGB and LAB colored  
179 NHL images. The features extracted from the original images, without data-  
180 augmentation, are given as input to a polynomial classifier. For binary class  
181 classification, an accuracy of up to 97% was obtained.

#### 182 *2.4. Gender and Age Classification*

183 Besides providing support to the diagnosis of diseases and differentiation  
184 of tumors, computer vision techniques applied on histological images can  
185 also serve as an indicator of age and gender. A set of images obtained from  
186 mice liver tissue has been explored recently for this task. In [3], the au-  
187 thors presented a novel deep learning approach named Texture-CNN. After  
188 applying this approach along with a voting classification scheme, accuracies  
189 of 99.1% and 98.2% were obtained for the classification of 2 gender and 4  
190 aging classes respectively. However, handcrafted features have also provided  
191 excellent results in this dataset. [12] applied 3 statistical approaches for grey  
192 texture analysis, testing on different color spaces. After using a SVM to  
193 classify the generated features, an accuracy of 100% was obtained for both  
194 gender and aging classes. More recently, the authors in [39] proposed an  
195 ensemble of handcrafted features and deep learning approaches. Moreover,  
196 new data augmentation techniques based on principal component analysis  
197 and discrete cosine transform were also presented. Using an ensemble of 6  
198 CNN models trained with different data augmentation approaches and a set  
199 of handcrafted features, the method was also able to obtain an accuracy of  
200 100% for classifying gender and age from liver histological images.

201 Despite providing relevant results, most of these methods were imple-  
202 mented for specific classification tasks. There are few computer vision ap-  
203 proaches that were able to perform well on different histological image cate-  
204 gories [48, 39, 19, 52]. Moreover, both handcrafted fractal features [46, 48, 49]  
205 and CNN models [31, 6, 3] were able to provide high accuracy rates in several  
206 CAD systems for histopathology tasks. Therefore, an ensemble method that  
207 addresses both fractal geometry and deep learning, which is the core of our

208 proposal, could be able to improve these results when applied to different  
209 histology datasets.

### 210 **3. Technical Background**

#### 211 *3.1. Fractal Features*

212 Fractal geometry is a concept designed for the study of shapes that could  
213 not be defined by euclidian geometry [35]. Shapes present in nature such as  
214 a coastline, clouds, trees or lightnings are examples of structures that don't  
215 have well-defined patterns. With fractal-based approaches, these structures  
216 can be represented by observations through different scales. In computer  
217 vision, such techniques are known as multiscale. Among the most common  
218 ones, we can highlight the box-counting [41] and the gliding-box [21] algo-  
219 rithms. The application of these algorithms consists in splitting the images  
220 onto different scales and then extracting features from each sub-image. For  
221 the representation of numerical features using fractal approaches, we have  
222 fractal dimension (FD), lacunarity (LAC) and percolation (PERC) as three  
223 of the most relevant. A multiscale and a multidimensional analysis of the  
224 image are performed in order to obtain these features.

225 One of the approaches available in the literature for multiscale analysis  
226 consists on the application of the gliding-box algorithm [21]. One of the main  
227 advantages of this approach is that it can be applied on datasets containing  
228 images with different resolutions, due to the fact that the output features are  
229 given in relation to the scale instead of being absolute values. This algorithm  
230 consists in placing a box  $\beta_i$  sized  $L \times L$  on the left superior corner of the  
231 image, wherein  $L$  is given in pixels. This box glides through the image, one  
232 column and then one row at a time. After reaching the end of the image, the  
233 box is repositioned at the starting point and the value of  $L$  is increased by  
234 2. On an image sized  $H \times W$ , the total number  $T$  of boxes  $\beta_i$  for a scale  $L$   
235 is given by Equation 1:

$$T(L) = (H - L + 1) \times (W - L + 1) \quad | \quad L \leq \min(H, W). \quad (1)$$

236 For each time the box  $\beta_i$  is moved, a multidimensional analysis of color  
237 similarity is performed for every pixel inside it. This is done by assigning the  
238 center pixel to a vector  $f_c = r_c, g_c, b_c$ , where  $r_c, g_c$  and  $b_c$  correspond to the  
239 color intensities of each of the RGB color channels of given pixel. The other  
240 pixels in the box are assigned to a vector  $f_i = r_i, g_i, b_i$  and compared to the

241 center pixel by calculating a color distance  $\Delta$ . On the proposed approach,  
 242 the Chessboard ( $\Delta_h$ ), Euclidian ( $\Delta_e$ ) and Manhattan ( $\Delta_m$ ) distances are  
 243 calculated according to Equations 2-4.

$$\Delta_h = \max(|f_i(k_i) - f_c(k_c)|), k \in r, g, b. \quad (2)$$

$$\Delta_e = \sqrt{\sum_k (f_i(k_i) - f_c(k_c))^2}, k \in r, g, b. \quad (3)$$

$$\Delta_m = \sum_k |f_i(k_i) - f_c(k_c)|, k \in r, g, b. \quad (4)$$

244 If the value of  $\Delta$  corresponding to the distance between  $f_i$  and  $f_c$  is less  
 245 than or equal to the scale  $L$ , then  $f_i$  is labeled as 1, otherwise  $f_i$  receives the  
 246 label 0. An example of the pixels' labelling when a distance  $\Delta$  is calculated  
 247 for a box sized  $3 \times 3$  is illustrated on Figure 1.

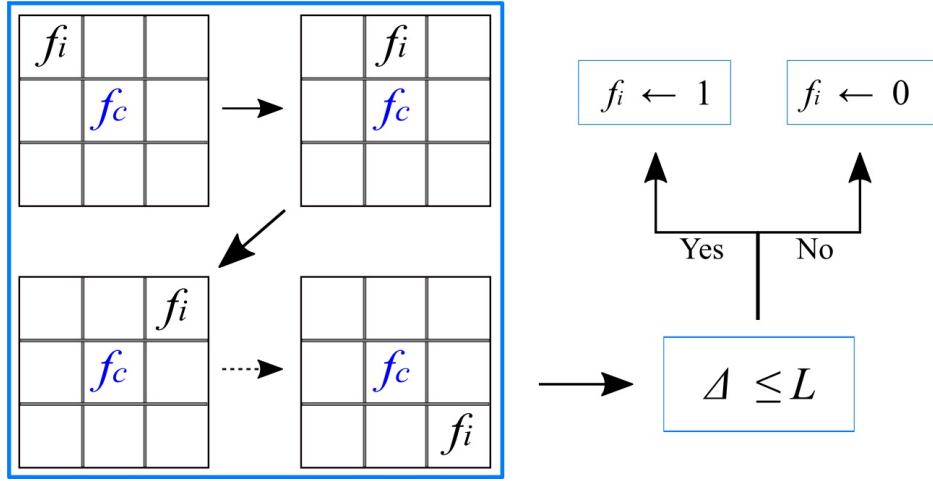


Figure 1: Labelling the pixels on a  $3 \times 3$  by calculating a distance  $\Delta$ .

248 This procedure converts a box that contains RGB values to one containing  
 249 binary values. After performing this conversion for every box of every given  
 250  $L$  scale, a structure known as probability matrix is generated. Each element  
 251 of the matrix corresponds to the probability  $P$  that  $m$  pixels on a scale  $L$   
 252 are labeled as 1 on each box. On Table 1, the visual representation of such  
 253 matrix is presented. The matrix is normalized in a way that the sum of the  
 254 elements in a column is equal to 1, as showed on Equation 5.

Table 1: Structure of the probability matrix.

	3	5	...	$L_{max}$
1	$P(1, 3)$	$P(1, 5)$	...	$P(1, L_{max})$
2	$P(2, 3)$	$P(2, 5)$	...	$P(2, L_{max})$
$\vdots$	$\vdots$	$\vdots$	$\ddots$	$\vdots$
$L^2$	$P(L^2, 3)$	$P(L^2, 5)$	...	$P(L^2, L_{max})$

$$\sum_{m=1}^{L^2} P(m, L) = 1, \forall L. \quad (5)$$

255 Noteworthy here that the probability matrix does not have the shape of  
 256 an ordinary rectangular matrix, as the number of rows grows exponentially  
 257 for each value of  $L$ . After the matrix is complete, the FD and LAC local  
 258 values can be obtained.

### 259 3.1.1. Fractal Dimension

260 FD is the most common technique to evaluate the fractal properties of an  
 261 image. This is a measure for evaluating the irregularity and the complexity  
 262 of a fractal.

263 To obtain local FD features from the probability matrix, for each value  
 264 of  $L$ , the FD denominated  $D(L)$  is calculated according to the Equation 6:

$$D(L) = \sum_{m=1}^{L^2} \frac{P(m, L)}{m}. \quad (6)$$

### 265 3.1.2. Lacunarity

266 LAC is a measure complementary to FD and allows to evaluate how the  
 267 space of a fractal is filled [20]. From the probability matrix, first and second  
 268 order moments are calculated with the Equations 7 and 8.

$$\mu(L) = \sum_{m=1}^{L^2} mP(m, L). \quad (7)$$

$$\mu^2(L) = \sum_{m=1}^{L^2} m^2P(m, L). \quad (8)$$

269 The value of LAC for a scale  $L$  is given by  $\Lambda(L)$ , which is obtained  
 270 according to the Equation 9:

$$\Lambda(L) = \frac{\mu^2(L) - (\mu(L))^2}{(\mu(L))^2}. \quad (9)$$

271 *3.1.3. Percolation*

272 PERC is a physical phenomenon that consists on the study of fluid prop-  
 273 erties on a porous media [15]. Such media is said to be percolating if a  
 274 fluid can flow through the whole system, from the top to the bottom. In  
 275 computer vision, this concept can be applied to verify the image porosity, or  
 276 some cluster properties regarding pixel neighborhoods [49]. The first steps  
 277 to obtain percolation features from a colored image follow the same proce-  
 278 dures described for obtaining FD and LAC features. After calculating  $\Delta$ , the  
 279 generated binary matrices are given as input to a cluster labelling algorithm.  
 280 Groups of nearby pixels that satisfied the criterion of the  $\Delta$  distance are  
 281 labelled in order to count the number of clusters on the image, as illustrated  
 282 in Figure 2. The symbol \* indicates pixels labelled as 1.

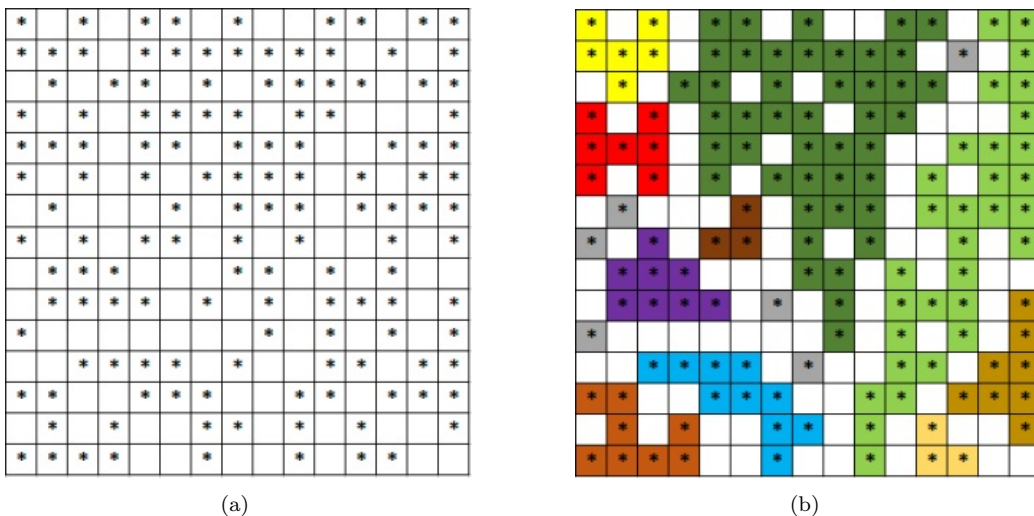


Figure 2: Matrix before (a) and after (b) the application of a cluster labelling algorithm.

283 Let  $c_i$  be the number of clusters on a box  $\beta_i$ , the feature  $C(L)$  that  
 284 represents the average number of clusters per box on a scale  $L$  is given by  
 285 Equation 10

$$C(L) = \frac{\sum_{i=1}^{T(L)} c_i}{T(L)}. \quad (10)$$

286 Another feature that can be obtained consists on the average coverage  
 287 area of the largest cluster in a box and is given by  $M(L)$ . Let  $m_i$  be the  
 288 size in pixels of the largest cluster of the box  $\beta_i$ . The feature  $M(L)$  is given  
 289 according to Equation 11:

$$M(L) = \frac{\sum_{i=1}^{T(L)} \frac{m_i}{L^2}}{T(L)}. \quad (11)$$

290 We can also verify whether a box  $\beta_i$  is percolating. This can be achieved  
 291 due to a property that states a percolation threshold for different types of  
 292 structures. In squared matrices (digital images), this threshold has the value  
 293 of  $p = 0.59275$  [8], which means that if the ratio between pixels labeled as 1  
 294 and pixels labeled as 0 is greater or equal than  $p$ , the matrix is considered as  
 295 percolating. Let  $\Omega_i$  be the number of pixels labeled as 1 in a box  $\beta_i$  with size  
 296  $L \times L$ , we determine whether such box is percolating according to Equation  
 297 12:

$$q_i = \begin{cases} 1, & \frac{\Omega_i}{L^2} \geq 0.59275. \\ 0, & \frac{\Omega_i}{L^2} < 0.59275. \end{cases} \quad (12)$$

298 This results in a binary value for  $q_i$ , wherein 1 indicates that the box is  
 299 percolating. The feature  $Q(L)$  regards the average occurrence of percolation  
 300 on a scale  $L$  and can be obtained as shown in Equation 13:

$$Q(L) = \frac{\sum_{i=1}^{T(L)} q_i}{T(L)}. \quad (13)$$

301 The number of obtained local features depends on the total of observation  
 302 scales  $L$ . Considering that  $L$  ranges from 3 to  $L_{max}$  with an increment of 2,  
 303 the amount of local features corresponds to  $5 \times (\frac{L_{max}-3}{2} + 1)$  for each  $\Delta$ . A  
 304 summary of these features is shown in Table 2.

### 305 3.2. Convolutional Neural Networks

306 CNN are a special type of deep learning model that learns features from  
 307 low- and high-level patterns on grid-shaped data [63]. The core of CNN

Table 2: Summary of the obtained local features.

<b>FD</b>	<b>LAC</b>	<b>PERC</b>		
$D(3)$	$\Lambda(3)$	$C(3)$	$Q(3)$	$M(3)$
$D(5)$	$\Lambda(5)$	$C(5)$	$Q(5)$	$M(5)$
$\vdots$	$\vdots$	$\vdots$	$\vdots$	$\vdots$
$D(L_{max})$	$\Lambda(L_{max})$	$C(L_{max})$	$Q(L_{max})$	$M(L_{max})$

308 are usually built from three types of layers: convolution; pooling; and fully  
 309 connected layers. While the first two perform feature extraction, the later  
 310 classifies these features and usually outputs a label to be assigned to the  
 311 input data.

312 The convolution layers are the base structures of the network, hence the  
 313 name CNN. These layers usually consist on a series of two operations. The  
 314 first is convolution, a simple linear procedure that performs element-wise  
 315 product between the input data and small arrays of numbers called kernels,  
 316 which are the only learnable parameters in this type of layers. The second  
 317 operation consists on passing the convolution output through a non-linear  
 318 activation function. Different functions have been applied, although the Rec-  
 319 tified Linear Unit (ReLU), which is given by  $f(x) = \max(0, x)$ , became the  
 320 most popular as it tends to reduce training time [30].

321 Pooling layers provides a downsampling operation that reduces the data  
 322 dimensionality. This is usually done by selecting the maximum or sometimes  
 323 the average value of an element in a patch and feeding it to the following  
 324 layer. These pooling operations are performed in order not only to decrease  
 325 the number of features but also to introduce a small invariance to translation  
 326 and distortion of structures in the input data.

327 The fully connected layers consist on a series of one or more layers wherein  
 328 every output is connected to every input of the following layer by a learnable  
 329 weight. Usually, the last fully connected layer has the same number of nodes  
 330 as the number of classes of the training dataset. In classification problems,  
 331 its output corresponds to class probabilities, which are obtained by applying  
 332 an activation function, such as softmax. The network’s prediction is given  
 333 by the class that obtained the highest probability value.

334 **4. Methodology**

335 *4.1. Image Databases*

336 We evaluated five histological image datasets. The first is the breast  
337 cancer dataset provided by the Center of Bio-Image Informatics from the  
338 University of California, Santa Barbara (UCSB) [14]. This dataset consists  
339 of 58 breast tissue images split into two groups: benign (32) and malignant  
340 (26). One example of each group is shown in Figure 3.

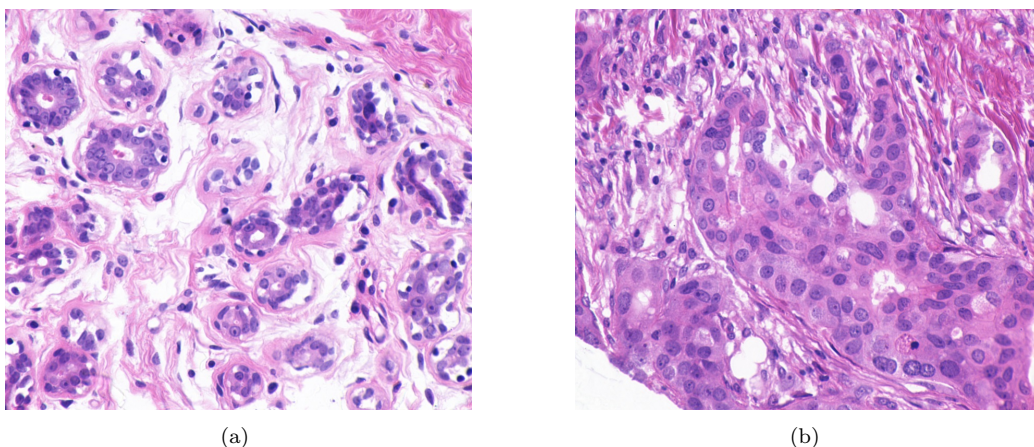


Figure 3: Samples of a benign (a) and a malignant (b) case from the UCSB dataset.

341 The second dataset (CR) consists of 165 colorectal tissue images [54], also  
342 split into benign (74) and malignant (91) tumors. To acquire the images,  
343 histological sections were digitally photographed with a Zeiss MIRAX MIDI  
344 Slide Scanner with a scaled pixel resolution of  $0.620\mu m$ , which corresponds to  
345 a magnification of 20x. On Figure 4, examples from each class are illustrated.

346 The third dataset (NHL) is composed by 173 non-Hodgkin Lymphoma  
347 images divided into three classes: MCL - mantle cell lymphoma (99); FL  
348 - follicular lymphoma (62); and CLL - chronic lymphocyte leukemia (12).  
349 For the acquisition of the images, a light microscope Zeiss Axioscope with  
350 a 20x objective and a colored digital camera (AXio Cam MR5) were used.  
351 The obtained images were recorded without compression, with a resolution  
352 of  $1388 \times 1040$  pixels, a 24 bit quantization ratio and the RGB color model.  
353 Regions of interest were later selected by a specialist [58]. This dataset was  
354 made publicly available by the National Cancer Institute and the National  
355 Institute on Aging [52].



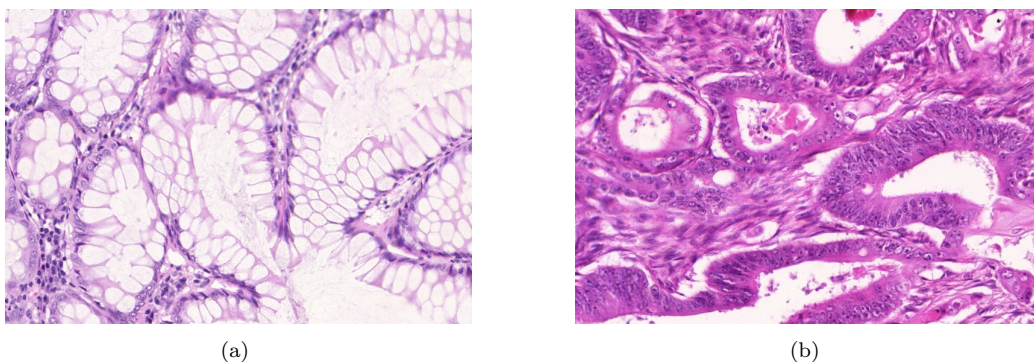


Figure 4: Samples of a benign (a) and a malignant (b) case from the CR dataset.

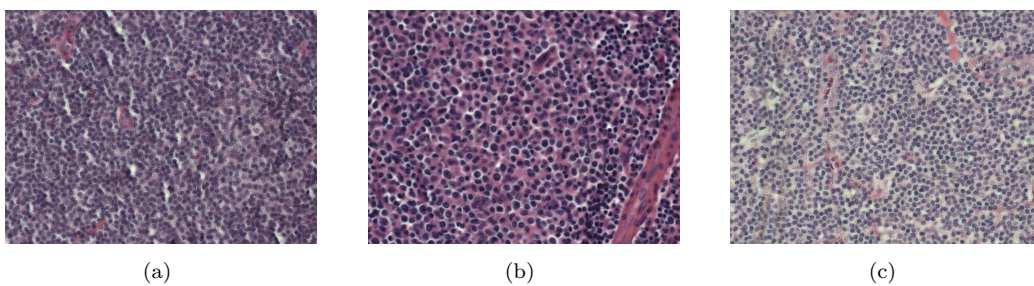
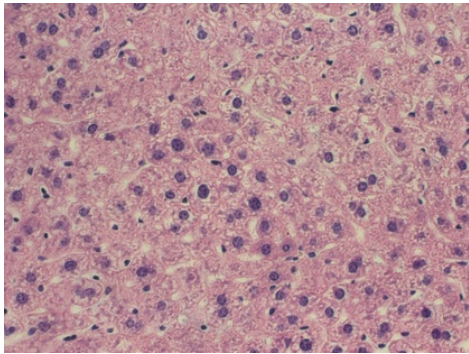
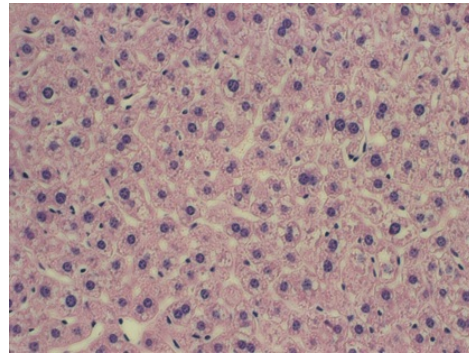


Figure 5: Samples of a CLL (a), a FL (b) and a MCL (c) case from the NHL dataset.

356 The two following datasets were both provided by the Atlas of Gene Ex-  
357 pression in Mouse Aging Project (AGEMAP) and are composed by liver  
358 tissue obtained from mice [42]. The images were acquired by a Carl Zeiss  
359 Axiovert 200 microscope and 40x objective. All images have the same res-  
360 olution of  $417 \times 312$  pixels. The fourth dataset (LG) consists of 265 liver  
361 tissue images obtained from male (150) and female (115) mice on a caloric  
362 restriction diet. Examples of each class are illustrated on Figure 6. The fifth  
363 dataset (LA) consists of 529 images split in four classes, wherein each repre-  
364 sents a different age group of female mice on ad-libitum diets: one (100), six  
365 (115), 16 (162) and 24 (152) months old. On Figure 7, one example of each  
366 age group is illustrated. An overview of all these datasets is presented on Ta-  
367 ble 3. In all five datasets, the tissue samples were stained with Hematoxylin  
368 and Eosin (H&E).

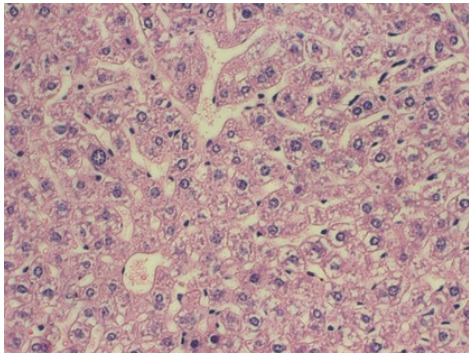


(a)

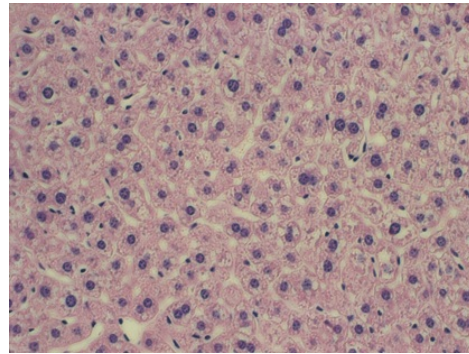


(b)

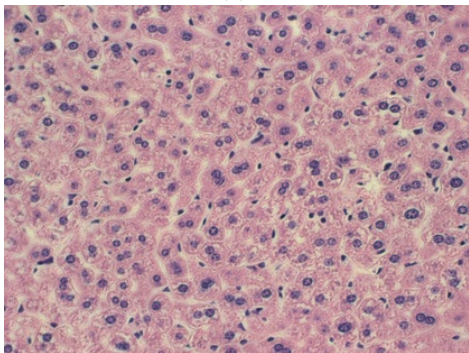
Figure 6: Samples of liver tissue from male (a) and female (b) mice from the LG dataset.



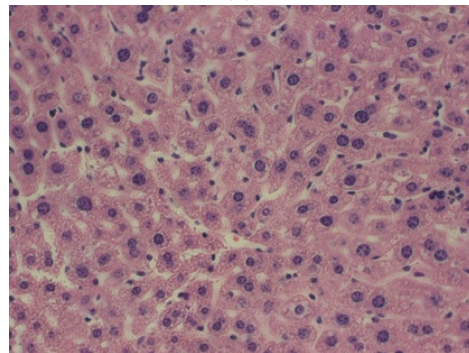
(a)



(b)



(c)



(d)

Figure 7: Samples of liver tissue from mice aged 1 month (a), 6 months (b), 16 months (c) and 24 months (d) from the LA dataset.

Table 3: Summary of the five tested datasets.

Dataset	Image	Classes	Samples	Resolution
UCSB [14]	Breast tumors	2	58	$896 \times 768$
CR [54]	Colorectal tumors	2	165	from $567 \times 430$ to $775 \times 522$
NHL [52]	Non-Hodgkin Lymphoma	3	173	from $86 \times 65$ to $1388 \times 1040$
LG [42]	Liver tissue	2	265	$417 \times 312$
LA [42]	Liver tissue	4	529	$417 \times 312$

369 *4.2. Method Overview*

370 The proposed approach can be split into two modules. The first module  
 371 performs the extraction of local features by applying the fractal techniques  
 372 described in Section 3.1. The output of this module consist on a set of 300  
 373 features, which were obtained from calculating the FD, LAC and PERC local  
 374 values from each of the three distances  $\Delta$  evaluated. The second module is  
 375 composed by 2 CNN whose goal is to perform classifications to obtain an  
 376 array of probabilities.

377 The input of the first CNN, henceforth named F-CNN, consists on an  
 378 artificial image generated from the features extracted on the first module.  
 379 The set of local features is reshaped into a  $10 \times 10 \times 3$  RGB image, which is a  
 380 procedure based on [33]. The generated images are given as input to a CNN  
 381 for classification. The second CNN, henceforth named O-CNN, receives as  
 382 input the original image, wherein the class probabilities obtained from the  
 383 classification of such image are summed to the respective class probabilities  
 384 from the F-CNN. After this sum, the highest probability value indicates the  
 385 class prediction. An overview of this approach is presented on Figure 8. Each  
 386 step is described in details on the following sections.

387 *4.3. Feature Extraction Module*

388 The main stage of the proposed method consists in applying the tech-  
 389 niques based on fractal geometry, described in Section 3.1, on the images  
 390 under investigation. FD, LAC, and PERC local features are extracted using  
 391 multiscale and multidimensional approaches.

392 After being given as input to the FNN, the image is divided into different  
 393 scales, according to the gliding-box algorithm. Each perceptron of the first  
 394 layer represents a different scale with value  $L$ . This layer’s function consists  
 395 simply in generating a set of matrices for every region of the image and every  
 396 assigned value of  $L$ , which ranges from 3 to 41 with an increment of 2. We  
 397 chose this value for  $L_{max}$  as it generates the exact number of features required

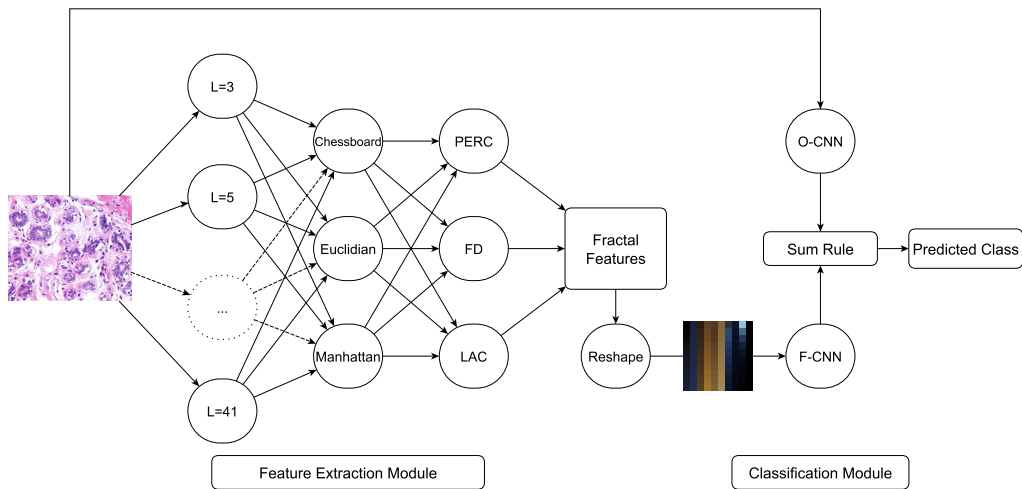


Figure 8: Overview of the proposed Fractal Neural Network model.

398 to provide a square image after applying the reshape procedure, which is  
 399 ideal to avoid distortions when feeding the image to the F-CNN, and also  
 400 due to the relevant classification results obtained with a similar value [46].  
 401 The generated matrices are given as input to the second layer, which is a  
 402 representation of the multidimensional approach of the methods described  
 403 on Section 3.1. In the proposed architecture, each perceptron performs the  
 404 calculation of a different type of distance  $\Delta$  between the pixels of the image.

405 The output of each perceptron in the second layer consists in a set of  
 406 binary matrices, wherein the values labeled as 1 are pixels that matched the  
 407  $\Delta$  criteria. These matrices are given as input to the perceptrons of the third  
 408 layer, wherein the techniques described on Section 3.1 for obtaining local FD,  
 409 LAC and PERC values are finally applied. The resulting output consists on  
 410 a set of 300 local features, which serve as input to the next module of the  
 411 network. Prior to being given as input to both CNN, the original and the  
 412 fractal images are resized in order to match the required input dimensions.

#### 413 4.4. Classification Module

414 On the proposed FNN, classification is performed by two CNN. Both  
 415 CNN are fine-tuned on the deepest layer, as we applied transfer learning  
 416 using models pre-trained on the ImageNet database [50] in order to increase  
 417 the accuracy whilst reducing the training time.

418 4.4.1. Fractal Features CNN - F-CNN

419 In order to serve as input for the incoming CNN classification, the feature  
 420 vectors generated on the previous layers of the network must be converted  
 421 into feature matrices. In order to do so, the set of 300 features obtained from  
 422 the calculation of each of the three distances  $\Delta$  are arranged to compose a  
 423 different dimension of the matrix, aiming to simulate RGB color channels.  
 424 Therefore, we split the feature vector into three sub-vectors containing 100  
 425 features. These features are sequentially rearranged into a  $10 \times 10$  matrix.  
 426 The matrices generated by  $\Delta_h$ ,  $\Delta_e$  and  $\Delta_m$  correspond to the R, G and B  
 427 color channels, respectively. In Figure 9, one example of each tested dataset  
 428 is shown in order to illustrate the reshaping procedure.

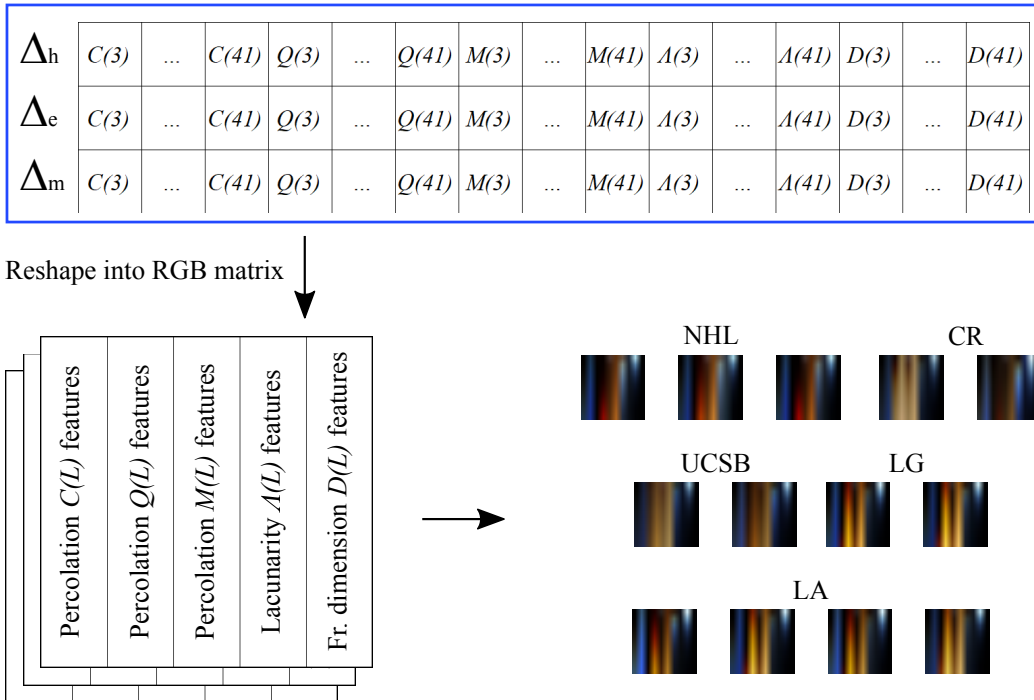


Figure 9: Illustration of the procedure to rearrange the local features in order to create a RGB image.

429 The generated images are given as input to the F-CNN, which outputs a  
 430 score vector for each image indicating class probabilities.

431 *4.4.2. Original Images CNN - O-CNN*

432 In order to fully explore the classification power of a CNN, we chose to  
 433 append a second CNN to the proposed architecture. The original images  
 434 are given as input to this CNN and the class probabilities obtained from the  
 435 output of the softmax layer are summed to the class probabilities obtained  
 436 from the correspondent layer of the F-CNN where the images generated from  
 437 fractal features were classified.

438 *4.4.3. Transfer Learning*

439 In order to reduce training time and achieve good results with few training  
 440 epochs we chose to use transfer learning instead of training both CNN from  
 441 scratch. Our proposed method applies network-based transfer learning [56],  
 442 wherein the pre-trained network is partially reused and only the final layer  
 443 is changed in order to match the number of classes. Therefore, we selected  
 444 four CNN candidates that have provided relevant results in histology image  
 445 classification recently [45, 34, 26] pre-trained on the ImageNet dataset. An  
 446 overview of these four models is shown in Table 4.

Table 4: Selected pre-trained CNN models.

Model	Layers	Parameters	Input size
ResNet-50 [16]	50	$2.6 \times 10^7$	$224 \times 224 \times 3$
ResNet-101 [16]	101	$4.5 \times 10^7$	$224 \times 224 \times 3$
InceptionV3 [55]	48	$2.4 \times 10^7$	$299 \times 299 \times 3$
Xception [9]	71	$2.3 \times 10^7$	$299 \times 299 \times 3$

447 *4.5. Performance Evaluation*

448 In order to obtain the best possible results with the proposed method and  
 449 properly evaluate these, we applied a testing approach divided in 4 stages.

450 Firstly, we evaluated which CNN model would be the most appropriate  
 451 for the F-CNN and O-CNN slots in the proposed architecture. Then, we  
 452 apply each of the CNN on the 5 datasets with the number of training epochs  
 453 ranging from 1 to 10. This verification aims to determine the smaller number  
 454 of epochs needed to obtain the highest accuracies. After these experiments,  
 455 the proposed approach is applied on the datasets using the configuration  
 456 results obtained from the previous tests. At last, we compare the proposed  
 457 method with other common feature extraction techniques, analysing results

Table 5: Loss evaluation of different CNN models and time performance in seconds.

Dataset		ResNet-50	ResNet-101	InceptionV3	Xception
NHL	F-CNN	0.510	0.494	0.478	<b>0.385</b>
	O-CNN	0.767	0.585	0.497	<b>0.409</b>
	Time	<b>42.69</b>	85.79	87.58	77.01
CR	F-CNN	0.350	0.312	0.339	<b>0.269</b>
	O-CNN	<b>0.018</b>	0.022	0.045	0.043
	Time	<b>50.21</b>	91.26	93.82	83.37
UCSB	F-CNN	0.567	0.741	0.621	<b>0.556</b>
	O-CNN	0.318	<b>0.271</b>	0.305	0.606
	Time	<b>21.99</b>	39.65	39.01	29.76
LG	F-CNN	0.163	<b>0.118</b>	0.151	<b>0.118</b>
	O-CNN	<b>0.005</b>	0.017	<b>0.005</b>	0.041
	Time	<b>67.25</b>	133.84	139.99	128.66
LA	F-CNN	<b>0.175</b>	0.189	0.196	0.193
	O-CNN	0.048	0.128	<b>0.031</b>	0.051
	Time	<b>122.47</b>	247.67	259.65	247.22

458 obtained from using only the F-CNN as well as the ensemble with the O-  
 459 CNN. To obtain these other features, we implemented the methods on Matlab  
 460 R2019b, applied them on the same datasets and performed classification  
 461 using the Rotation Forest classifier available at the software Weka 3.6.13. We  
 462 chose this classifier due to its relevant results obtained from other researches  
 463 on histology image classification [1, 48].

464 All tests were performed on a Intel Xeon Silver 4116 CPU at 2.10GHz  
 465 with 128GB of RAM and a NVIDIA GeForce RTX 2080Ti embedded, using  
 466 Matlab R2019b. Since some of the tested datasets have a small number of  
 467 samples, we chose to apply 10-folds cross-validation in all testing stages in  
 468 order to avoid problems such as overfitting.

## 469 5. Results and Discussion

470 Before testing the proposed model on its complete implementation, it was  
 471 necessary to determine the CNN models to be assigned to the F-CNN and  
 472 O-CNN slots. We tested the performance of four of the most popular CNN  
 473 that have been applied on recent researches. On Table 5, the loss values for  
 474 each dataset are presented as well as the average time in seconds required to  
 475 train and classify the samples in 10 epochs.

476 We applied the Friedman non-parametrical test to verify whether the  
 477 difference among the loss values were significant [23]. At  $\alpha = 0.05$ , we

Table 6: Accuracy values for the F-CNN with varying training epochs.

Epochs	NHL	CR	UCSB	LG	LA	Avg.
1	78.03%	77.58%	60.34%	68.68%	77.88%	72.50%
2	80.35%	78.79%	70.69%	81.13%	81.66%	78.52%
3	78.61%	83.03%	68.97%	91.32%	84.88%	81.36%
4	82.66%	83.64%	70.69%	88.68%	86.39%	82.41%
5	<b>84.97%</b>	<b>89.09%</b>	74.14%	93.21%	86.77%	85.63%
6	84.39%	86.67%	72.41%	89.81%	91.68%	84.99%
7	<b>84.97%</b>	88.48%	68.97%	90.94%	91.68%	85.01%
8	84.39%	88.48%	72.41%	91.70%	90.36%	85.47%
9	82.66%	86.06%	<b>79.31%</b>	95.09%	<b>93.57%</b>	<b>87.34%</b>
10	83.81%	86.06%	77.59%	<b>95.47%</b>	93.19%	87.23%

Table 7: Accuracy values for the O-CNN with varying training epochs.

Epochs	NHL	CR	UCSB	LG	LA	Avg.
1	83.82%	93.33%	56.90%	98.49%	92.82%	85.07%
2	87.28%	98.18%	58.62%	98.49%	95.27%	87.57%
3	89.02%	98.79%	68.97%	98.49%	96.03%	90.26%
4	90.75%	98.78%	72.41%	98.11%	96.68%	91.33%
5	90.75%	<b>100.00%</b>	75.86%	<b>99.62%</b>	98.11%	92.87%
6	88.44%	99.39%	79.31%	<b>99.62%</b>	97.16%	92.79%
7	90.17%	99.39%	74.14%	<b>99.62%</b>	98.49%	92.36%
8	<b>93.64%</b>	98.79%	81.03%	98.87%	98.68%	<b>94.20%</b>
9	89.60%	98.18%	<b>82.76%</b>	98.87%	99.05%	93.69%
10	88.44%	99.39%	75.86%	98.82%	<b>99.43%</b>	92.40%

478 obtained  $P_k = 0.2073$  for the F-CNN and  $P_k = 0.4144$  for the O-CNN, which  
 479 indicates that there is not a significant difference when comparing the four  
 480 tested CNN models. However, when comparing the time needed to perform  
 481 training, the Friedman test indicated a significant difference ( $P_k < 0.0001$ )  
 482 for all pairwise comparisons (Conover) involving the ResNet-50. Therefore,  
 483 we chose the ResNet-50 to be assigned to both CNN slots of our proposed  
 484 architecture not only due to its shorter training time, but also due to the  
 485 relevant results recently obtained in the classification of histology images  
 486 [45, 34, 60, 61].

487 Then, we tested the performance of each of the two CNN varying the  
 488 number of training epochs. To prevent overfitting, and aiming to build a  
 489 fast-training model, we chose to not go beyond 10 epochs for both CNN.  
 490 The results are shown in Tables 6 and 7 for the F-CNN and the O-CNN  
 491 respectively.



Table 8: Results obtained from the application of the proposed method.

	Accuracy	F-score
NHL	95.55%	0.864
CR	99.39%	0.994
UCSB	89.66%	0.895
LG	99.62%	0.996
LA	99.62%	0.996
Avg.	96.77%	0.949
SD.	4.334	0.058

492 From the results presented on Tables 6 and 7, it can be noted that the  
 493 F-CNN is able to provide relevant results after 4 epochs. On the other hand,  
 494 the O-CNN presented significant performance values with only 2 training  
 495 epochs, providing accuracies above 85% for all datasets, with an exception for  
 496 the breast tumor images, due to its small number of samples. Nevertheless,  
 497 the best results were obtained with 9 and 8 training epochs for the F-CNN  
 498 and O-CNN respectively. Therefore, these parameters were applied on the  
 499 following tests.

500 We proceeded to apply the proposed FNN using the configuration pa-  
 501 rameters obtained on the previous tests in order to evaluate the performance  
 502 when applied to the five histology images dataset. The detailed results are  
 503 shown on Table 8.

504 These results show that the proposed method is able to perform well on  
 505 the classification of histology images. With exception for the UCSB dataset,  
 506 accuracies above 95% were obtained, which can be a indicator of the method’s  
 507 adaptability to different categories of histological tissue. Despite dealing with  
 508 imbalanced classes on all datasets, the proposed method was also able to  
 509 provide F-Measure values above 0.850 in all cases. It is also noteworthy the  
 510 excellent results obtained for the CR, LG and LA, with performance values  
 511 close to 1.0 for all evaluated metrics.

512 In order to verify how the proposed method fits among other computer  
 513 vision approaches, we compare its performance with the results obtained by  
 514 LBP, Haralick, PERC, LAC and FD features. It’s important to highlight  
 515 that the fractal features used for comparison in this test consist of common  
 516 feature vectors that are given as input to machine learning algorithms, which  
 517 differs from our approach of reshaping the fractal features into a RGB image  
 518 and feeding it to a CNN. Firstly, we compared the individual performance of

Table 9: Accuracy values obtained by different computer vision methods.

	NHL	CR	UCSB	LG	LA
LBP	72.83%	67.27%	79.31%	80.75%	71.46%
Haralick	74.57%	73.94%	81.03%	89.43%	88.28%
PERC	<b>93.64%</b>	87.27%	<b>82.76%</b>	95.09%	93.57%
LAC	89.60%	66.67%	79.31%	86.04%	83.93%
FD	78.03%	59.39%	62.07%	58.49%	50.47%
F-CNN	82.66%	86.06%	79.31%	95.09%	93.57%
O-CNN	<b>93.64%</b>	<b>98.79%</b>	81.03%	<b>98.87%</b>	<b>98.68%</b>

Table 10: Accuracy values obtained by the application of a classification ensemble between the O-CNN and other techniques.

	NHL	CR	UCSB	LG	LA
LBP	83.24%	91.52%	82.76%	93.58%	89.41%
Haralick	87.28%	92.12%	82.76%	95.47%	92.25%
PERC	94.22%	97.58%	86.21%	<b>99.62%</b>	99.24%
LAC	94.22%	98.18%	86.21%	<b>99.62%</b>	98.87%
FD	91.91%	98.79%	82.76%	99.25%	99.05%
FNN	<b>95.55%</b>	<b>99.39%</b>	<b>89.66%</b>	<b>99.62%</b>	<b>99.62%</b>

519 these techniques without using any classification fusion or ensemble approach.  
 520 Thus, we did not performed the ensemble scheme between the F-CNN and  
 521 the O-CNN, as it is originally intended for our proposal. The results are  
 522 shown in Table 9.

523 Without using any ensemble approach, the O-CNN, which consists simply  
 524 on using a ResNet-50 for classifying the original images, provided the best  
 525 results. An exception is made for the UCSB dataset, wherein the best results  
 526 were provided by the PERC features. Moreover, apart from the FD, the  
 527 fractal features performed better than the LBP and Haralick descriptors in  
 528 most cases. It can also be noted that the proposed F-CNN struggles to  
 529 provide relevant results when applied on its own.

530 Thus, our method implements an ensemble between the F-CNN and the  
 531 O-CNN. However, since a comparison among an ensemble method and non-  
 532 ensemble approaches would not be fair, we included the O-CNN classification  
 533 to compose an ensemble with the other compared methods. These results  
 534 are shown in Table 10.

535 It can be noted that merging the classification results of both CNN not  
 536 only improves the accuracy of the F-CNN, but also enhances the performance  
 537 of the O-CNN. When compared to the other techniques, the proposed method  
 538 provided better accuracies in all datasets. The LG dataset was the only  
 539 one where the results obtained by our method could be matched by other  
 540 techniques. In this case, the same accuracy value of 99.62% was obtained  
 541 by PERC, LAC and the FNN. Besides, a significant difference among the  
 542 compared techniques was indicated according to the Friedman test ( $P_k <$   
 543  $0.0001$  for  $\alpha = 0.05$ ) in all pairwise comparisons (Conover). Our method  
 544 also provided the highest average accuracy (96.8%) and smallest standard  
 545 deviation (4.334), as can be seen on the graph presented on Figure 10.

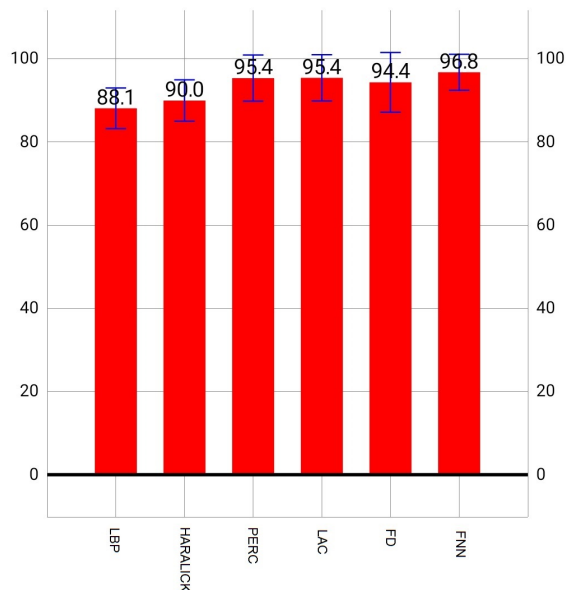


Figure 10: Average accuracy of the evaluated classification ensemble between the O-CNN and other techniques, applied to the five tested datasets.

546 An overview of the results obtained with the FNN in relation to other  
 547 approaches in the context of histology image classification is shown in Table  
 548 11. It can be noted that the methods that provided the best results on each  
 549 classification task applied both deep learning (DL) and handcrafted (HC)  
 550 features. Regarding the FNN, we were able to verify that its performance is  
 551 compatible with recently published methods. Breast and colorectal cancer

552 classification remains as a challenging task in computer vision, since few  
553 methods were able to obtain accuracies above 95% when classifying these  
554 type of images. Nevertheless the FNN was able to achieve a remarkable  
555 99.39% accuracy, ranking first among the compared methods in colorectal  
556 cancer classification.

## 557 **6. Conclusion**

558 In this paper, we proposed an approach (FNN) that consists on the en-  
559 semble of two CNN, wherein one of these receives as input images generated  
560 from fractal features, to classify different categories of histological images.  
561 We showed that our proposal was able to provide relevant results, with accu-  
562 racies above 89%, for all tested histopathology challenges. Also, accuracies  
563 greater than 99% were obtained for three out of the five evaluated datasets  
564 (CR, LG and LA). Besides, we achieved these results with a training time  
565 shorter than the required for other approaches such as [64, 51, 29] to obtain  
566 similar performances. Therefore, we believe our proposal contributes to this  
567 research area not only due to its adaptability to different types of histol-  
568 ogy tissue and relatively low computing cost, but mainly due to the applied  
569 feature vectors reshaping concept that allows the combined use of fractal fea-  
570 tures and CNN. This approach has not yet been deeply explored and could  
571 provide new insights on the combined power of handcrafted features and  
572 deep learning. Nevertheless, there is still room for improvement, specially in  
573 regard to the UCSB dataset classification, wherein hyper-parameter tuning  
574 could play a major role to improve the model’s accuracy.

575 For future works, we propose the application of the FNN on other types  
576 of histology tissue images, a study for optimizing the F-CNN and the O-  
577 CNN parameters, the inclusion of fractal global features in the classification  
578 ensemble and a deeper analysis of the fractal features reshaping procedure,  
579 *e.g.* experimenting different ways to dispose the features or generating images  
580 using a different 3-channel color model.

## 581 **7. Acknowledgment**

582 This study was financed in part by the Coordenação de Aperfeiçoamento  
583 de Pessoal de Nível Superior - Brasil (CAPES) - Finance Code 001 and by  
584 the Programa Institucional de Internacionalização (PRINT/CAPES, Brazil),  
585 project #88882.461704/2019-01. The authors gratefully acknowledge the

Table 11: Overview of the accuracy values obtained by different approaches in the context of histology image classification.

Images	Method	Approach	Accuracy
NHL	[6]	DL+HC	99,10%
	[24]	DL	97,96%
	[36]	HC	97,00%
	[22]	DL	96,58%
	<b>FNN</b>	DL+HC	<b>95,55%</b>
	[47]	HC	86,14%
Breast	[31]	DL+HC	100,00%
	[64]	DL+HC	96,67%
	[13]	DL	94,41%
	[29]	DL	91,00%
	<b>FNN</b>	DL+HC	<b>89,66%</b>
	[48]	HC	86,20%
	[44]	DL	84,67%
	[4]	DL	83,30%
Colorectal	[38]	HC	80,00%
	<b>FNN</b>	DL+HC	<b>99,39%</b>
	[11]	DL	96,97%
	[57]	DL	94,02%
	[51]	DL	93,28%
	[48]	HC	90,90%
	[7]	DL	87,50%
Liver (gender)	[5]	DL	85,00%
	[39]	DL+HC	100,00%
	[12]	HC	100,00%
Liver (age)	<b>FNN</b>	DL+HC	<b>99,62%</b>
	[3]	DL	99,10%
	[39]	DL+HC	100,00%
Liver (age)	[12]	HC	100,00%
	<b>FNN</b>	DL+HC	<b>99,62%</b>
	[3]	DL	98,20%

586 financial support of National Council for Scientific and Technological De-  
587 velopment CNPq (Grant #427114/2016-0, Grant #304848/2018-2, Grant  
588 #430965/2018-4 and Grant #313365/2018-0) and the State of Minas Gerais

589 Research Foundation - FAPEMIG (Grant #APQ-00578-18).

## 590 **References**

- 591 [1] Aličković, E., Subasi, A., 2017. Breast cancer diagnosis using ga feature  
592 selection and rotation forest. *Neural Computing and Applications* 28 (4),  
593 753–763.
- 594 [2] Amalina, N. N., Ramadhani, K. N., Sthevanie, F., 2019. Nuclei detection  
595 and classification system based on speeded up robust feature (surf).  
596 *EMITTER International Journal of Engineering Technology* 7 (1), 1–  
597 13.
- 598 [3] Andrearczyk, V., Whelan, P. F., 2017. Deep learning for biomedical  
599 texture image analysis. In: *Proceedings of the Irish Machine Vision &*  
600 *Image Processing Conference. Irish Pattern Recognition & Classification*  
601 *Society (IPRCS)*.
- 602 [4] Araújo, T., Aresta, G., Castro, E., Rouco, J., Aguiar, P., Eloy, C.,  
603 Polónia, A., Campilho, A., 2017. Classification of breast cancer histology  
604 images using convolutional neural networks. *PloS one* 12 (6).
- 605 [5] Awan, R., Al-Maadeed, S., Al-Saady, R., Bouridane, A., 2019. Glandu-  
606 lar structure-guided classification of microscopic colorectal images using  
607 deep learning. *Computers & Electrical Engineering*, 106450.
- 608 [6] Bai, J., Jiang, H., Li, S., Ma, X., 2019. Nhl pathological image clas-  
609 sification based on hierarchical local information and googlenet-based  
610 representations. *BioMed research international* 2019.
- 611 [7] Bentaieb, A., Hamarneh, G., 2018. Adversarial stain transfer for  
612 histopathology image analysis. *IEEE transactions on medical imaging*  
613 37 (3), 792–802.
- 614 [8] Bird, N., Perrier, E., 2010. Multiscale percolation properties of a fractal  
615 pore network. *Geoderma* 160 (1), 105–110.
- 616 [9] Chollet, F., 2017. Xception: Deep learning with depthwise separable  
617 convolutions. In: *Proceedings of the IEEE conference on computer vision*  
618 *and pattern recognition*. pp. 1251–1258.

- 619 [10] Cireşan, D. C., Giusti, A., Gambardella, L. M., Schmidhuber, J., 2013.  
620 Mitosis detection in breast cancer histology images with deep neural  
621 networks. In: International conference on medical image computing and  
622 computer-assisted intervention. Springer, pp. 411–418.
- 623 [11] Dabass, M., Vig, R., Vashisth, S., 2019. Five-grade cancer classification  
624 of colon histology images via deep learning. In: Communication and  
625 Computing Systems: Proceedings of the 2nd International Conference  
626 on Communication and Computing Systems (ICCCS 2018), December  
627 1-2, 2018, Gurgaon, India. CRC Press, p. 18.
- 628 [12] Di Ruberto, C., Putzu, L., Arabnia, H., Quoc-Nam, T., 2016. A fea-  
629 ture learning framework for histology images classification. In: Emerg-  
630 ing trends in applications and infrastructures for computational biology,  
631 bioinformatics, and systems biology: systems and applications. Elsevier  
632 Press, pp. 37–48.
- 633 [13] Feng, Y., Zhang, L., Yi, Z., 2018. Breast cancer cell nuclei classifica-  
634 tion in histopathology images using deep neural networks. International  
635 journal of computer assisted radiology and surgery 13 (2), 179–191.
- 636 [14] Gelasca, E. D., Byun, J., Obara, B., Manjunath, B., Oct 2008. Evalua-  
637 tion and benchmark for biological image segmentation. In: IEEE Inter-  
638 national Conference on Image Processing.
- 639 [15] Ghanbarian, B., Hunt, A. G., Skinner, T. E., Ewing, R. P., 2015. Satu-  
640 ration dependence of transport in porous media predicted by percolation  
641 and effective medium theories. Fractals 23 (01), 1540004.
- 642 [16] He, K., Zhang, X., Ren, S., Sun, J., 2016. Deep residual learning for  
643 image recognition. In: Proceedings of the IEEE conference on computer  
644 vision and pattern recognition. pp. 770–778.
- 645 [17] Howlader, N., Noone, A., Krapcho, M., Miller, D., Bishop, K., Kosary,  
646 C., Yu, M., Ruhl, J., Tatalovich, Z., Mariotto, A., et al., 2017. Seer  
647 cancer statistics review, 1975-2014, national cancer institute. Bethesda,  
648 MD, 1–12.
- 649 [18] Huang, Q., Zhang, F., Li, X., 2018. Machine learning in ultrasound  
650 computer-aided diagnostic systems: a survey. BioMed research interna-  
651 tional 2018.

- 652 [19] Ilse, M., Tomczak, J. M., Welling, M., 2018. Attention-based deep mul-  
653 tiple instance learning. In: 35th International Conference on Machine  
654 Learning, ICML 2018. International Machine Learning Society (IMLS),  
655 pp. 3376–3391.
- 656 [20] Ivanovici, M., Richard, N., 2009. The lacunarity of colour fractal images.  
657 In: Image Processing (ICIP), 2009 16th IEEE International Conference  
658 on. IEEE, pp. 453–456.
- 659 [21] Ivanovici, M., Richard, N., 2011. Fractal dimension of color fractal im-  
660 ages. IEEE Transactions on Image Processing 20 (1), 227–235.
- 661 [22] Janowczyk, A., Madabhushi, A., 2016. Deep learning for digital pathol-  
662 ogy image analysis: A comprehensive tutorial with selected use cases.  
663 Journal of pathology informatics 7.
- 664 [23] Japkowicz, N., Shah, M., 2011. Evaluating learning algorithms: a clas-  
665 sification perspective. Cambridge University Press.
- 666 [24] Jiang, C., Su, J., 2018. Gabor binary layer in convolutional neural net-  
667 works. In: 2018 25th IEEE International Conference on Image Process-  
668 ing (ICIP). IEEE, pp. 3408–3412.
- 669 [25] Jiang, H., Li, Z., Li, S., Zhou, F., 2018. An effective multi-classification  
670 method for nhl pathological images. In: 2018 IEEE International Con-  
671 ference on Systems, Man, and Cybernetics (SMC). IEEE, pp. 763–768.
- 672 [26] Jiang, Y., Chen, L., Zhang, H., Xiao, X., 2019. Classification of h&e  
673 stained breast cancer histopathology images based on convolutional neu-  
674 ral network. In: Journal of Physics: Conference Series. Vol. 1302. IOP  
675 Publishing, p. 032018.
- 676 [27] Jothi, J. A. A., Rajam, V. M. A., 2017. A survey on automated can-  
677 cer diagnosis from histopathology images. Artificial Intelligence Review  
678 48 (1), 31–81.
- 679 [28] Juefei-Xu, F., Naresh Boddeti, V., Savvides, M., 2017. Local binary  
680 convolutional neural networks. In: Proceedings of the IEEE conference  
681 on computer vision and pattern recognition. pp. 19–28.



- 682 [29] Kausar, T., Wang, M., Idrees, M., Lu, Y., 2019. Hwdcnn: Multi-class  
683 recognition in breast histopathology with haar wavelet decomposed im-  
684 age based convolution neural network. *Biocybernetics and Biomedical*  
685 *Engineering* 39 (4), 967–982.
- 686 [30] Krizhevsky, A., Sutskever, I., Hinton, G. E., 2012. Imagenet classifica-  
687 tion with deep convolutional neural networks. In: *Advances in neural*  
688 *information processing systems*. pp. 1097–1105.
- 689 [31] Li, Y., Xie, X., Shen, L., Liu, S., 2019. Reverse active learning based  
690 atrous densenet for pathological image classification. *BMC bioinformat-*  
691 *ics* 20 (1), 445.
- 692 [32] Liu, L., Chen, J., Fieguth, P., Zhao, G., Chellappa, R., Pietikainen,  
693 M., 2018. A survey of recent advances in texture representation. *arXiv*  
694 *preprint arXiv:1801.10324* 3.
- 695 [33] Lumini, A., Nanni, L., 2018. Convolutional neural networks for atc clas-  
696 sification. *Current pharmaceutical design* 24 (34), 4007–4012.
- 697 [34] Mahbod, A., Ellinger, I., Ecker, R., Smedby, Ö., Wang, C., 2018. Breast  
698 cancer histological image classification using fine-tuned deep network  
699 fusion. In: *International Conference Image Analysis and Recognition*.  
700 Springer, pp. 754–762.
- 701 [35] Mandelbrot, B. B., 1975. *Les objets fractals: forme, hasard et dimension*.
- 702 [36] Martins, A. S., Neves, L. A., Faria, P. R., Tosta, T. A., Bruno, D. O.,  
703 Longo, L. C., do Nascimento, M. Z., 2019. Colour feature extraction  
704 and polynomial algorithm for classification of lymphoma images. In:  
705 *Iberoamerican Congress on Pattern Recognition*. Springer, pp. 262–271.
- 706 [37] Mohammed, M. A., Al-Khateeb, B., Rashid, A. N., Ibrahim, D. A.,  
707 Ghani, M. K. A., Mostafa, S. A., 2018. Neural network and multi-fractal  
708 dimension features for breast cancer classification from ultrasound im-  
709 ages. *Computers & Electrical Engineering* 70, 871–882.
- 710 [38] Mueller, J. L., Gallagher, J. E., Chitalia, R., Krieger, M., Erkanli, A.,  
711 Willett, R. M., Geradts, J., Ramanujam, N., 2016. Rapid staining and  
712 imaging of subnuclear features to differentiate between malignant and

- 713 benign breast tissues at a point-of-care setting. *Journal of cancer re-*  
714 *search and clinical oncology* 142 (7), 1475–1486.
- 715 [39] Nanni, L., Brahnam, S., Ghidoni, S., Maguolo, G., 2019. General pur-  
716 pose (genp) bioimage ensemble of handcrafted and learned features with  
717 data augmentation. arXiv preprint arXiv:1904.08084.
- 718 [40] Nanni, L., Ghidoni, S., Brahnam, S., 2017. Handcrafted vs. non-  
719 handcrafted features for computer vision classification. *Pattern Recog-*  
720 *nition* 71, 158–172.
- 721 [41] Nikolaidis, N., Nikolaidis, I., Tsouros, C., 2011. A variation of  
722 the box-counting algorithm applied to colour images. arXiv preprint  
723 arXiv:1107.2336.
- 724 [42] on Aging, N. I., Accessed: 2020-05-04. The atlas of gene expression  
725 in mouse aging project (agemap). [https://ome.grc.nia.nih.gov/](https://ome.grc.nia.nih.gov/iicbu2008/agemap/index.html)  
726 [iicbu2008/agemap/index.html](https://ome.grc.nia.nih.gov/iicbu2008/agemap/index.html).
- 727 [43] Orlov, N. V., Chen, W. W., Eckley, D. M., Macura, T. J., Shamir,  
728 L., Jaffe, E. S., Goldberg, I. G., 2010. Automatic classification of lym-  
729 phoma images with transform-based global features. *IEEE Transactions*  
730 *on Information Technology in Biomedicine* 14 (4), 1003–1013.
- 731 [44] Papastergiou, T., Zacharaki, E. I., Megalooikonomou, V., 2018. Tensor  
732 decomposition for multiple-instance classification of high-order medical  
733 data. *Complexity* 2018.
- 734 [45] Rakhlin, A., Shvets, A., Iglovikov, V., Kalinin, A. A., 2018. Deep con-  
735 volutional neural networks for breast cancer histology image analysis.  
736 In: *International Conference Image Analysis and Recognition*. Springer,  
737 pp. 737–744.
- 738 [46] Ribeiro, M. G., Neves, L. A., do Nascimento, M. Z., Roberto, G. F.,  
739 Martins, A. S., Tosta, T. A. A., 2019. Classification of colorectal can-  
740 cer based on the association of multidimensional and multiresolution  
741 features. *Expert Systems with Applications* 120, 262–278.
- 742 [47] Ribeiro, M. G., Neves, L. A., Roberto, G. F., Tosta, T. A., Martins,  
743 A. S., do Nascimento, M. Z., 2018. Analysis of the influence of color  
744 normalization in the classification of non-hodgkin lymphoma images.

- 745 In: 2018 31st SIBGRAPI Conference on Graphics, Patterns and Images  
746 (SIBGRAPI). IEEE, pp. 369–376.
- 747 [48] Roberto, G. F., Nascimento, M. Z., Martins, A. S., Tosta, T. A., Faria,  
748 P. R., Neves, L. A., 2019. Classification of breast and colorectal tumors  
749 based on percolation of color normalized images. *Computers & Graphics*  
750 84, 134–143.
- 751 [49] Roberto, G. F., Neves, L. A., Nascimento, M. Z., Tosta, T. A., Longo,  
752 L. C., Martins, A. S., Faria, P. R., 2017. Features based on the perco-  
753 lation theory for quantification of non-hodgkin lymphomas. *Computers*  
754 *in biology and medicine* 91, 135–147.
- 755 [50] Russakovsky, O., Deng, J., Su, H., Krause, J., Satheesh, S., Ma, S.,  
756 Huang, Z., Karpathy, A., Khosla, A., Bernstein, M., et al., 2015. Im-  
757 agenet large scale visual recognition challenge. *International journal of*  
758 *computer vision* 115 (3), 211–252.
- 759 [51] Sena, P., Fioresi, R., Faglioni, F., Losi, L., Faglioni, G., Roncucci, L.,  
760 2019. Deep learning techniques for detecting preneoplastic and neoplas-  
761 tic lesions in human colorectal histological images. *Oncology Letters*  
762 18 (6), 6101–6107.
- 763 [52] Shamir, L., Orlov, N., Eckley, D. M., Macura, T. J., Goldberg, I. G.,  
764 2008. Iicbu 2008: a proposed benchmark suite for biological image anal-  
765 ysis. *Medical & biological engineering & computing* 46 (9), 943–947.
- 766 [53] Simon, O., Yacoub, R., Jain, S., Tomaszewski, J. E., Sarder, P., 2018.  
767 Multi-radial lbp features as a tool for rapid glomerular detection and  
768 assessment in whole slide histopathology images. *Scientific reports* 8 (1),  
769 2032.
- 770 [54] Sirinukunwattana, K., Pluim, J. P., Chen, H., Qi, X., Heng, P.-A., Guo,  
771 Y. B., Wang, L. Y., Matuszewski, B. J., Bruni, E., Sanchez, U., et al.,  
772 2017. Gland segmentation in colon histology images: The glas challenge  
773 contest. *Medical image analysis* 35, 489–502.
- 774 [55] Szegedy, C., Vanhoucke, V., Ioffe, S., Shlens, J., Wojna, Z., 2016. Re-  
775 thinking the inception architecture for computer vision. In: *Proceedings*  
776 *of the IEEE conference on computer vision and pattern recognition*. pp.  
777 2818–2826.

- 778 [56] Tan, C., Sun, F., Kong, T., Zhang, W., Yang, C., Liu, C., 2018. A sur-  
779 vey on deep transfer learning. In: International conference on artificial  
780 neural networks. Springer, pp. 270–279.
- 781 [57] Tavolara, T. E., Niazi, M. K. K., Arole, V., Chen, W., Frankel, W., Gur-  
782 can, M. N., 2019. A modular cgan classification framework: Application  
783 to colorectal tumor detection. *Scientific Reports* 9 (1), 1–8.
- 784 [58] Tosta, T. A. A., Faria, P. R., Neves, L. A., do Nascimento, M. Z., 2017.  
785 Computational method for unsupervised segmentation of lymphoma his-  
786 tological images based on fuzzy 3-partition entropy and genetic algo-  
787 rithm. *Expert Systems with Applications* 81, 223–243.
- 788 [59] Wang, H., Roa, A. C., Basavanahally, A. N., Gilmore, H. L., Shih, N.,  
789 Feldman, M., Tomaszewski, J., Gonzalez, F., Madabhushi, A., 2014. Mi-  
790 tosis detection in breast cancer pathology images by combining hand-  
791 crafted and convolutional neural network features. *Journal of Medical*  
792 *Imaging* 1 (3), 034003.
- 793 [60] Wang, Y., Huang, F., Zhang, Y., Zhang, R., Lei, B., Wang, T., 2019.  
794 Breast cancer image classification via multi-level dual-network features  
795 and sparse multi-relation regularized learning. In: 2019 41st Annual In-  
796 ternational Conference of the IEEE Engineering in Medicine and Biology  
797 Society (EMBC). IEEE, pp. 7023–7026.
- 798 [61] Wang, Y., Lei, B., Elazab, A., Tan, E.-L., Wang, W., Huang, F., Gong,  
799 X., Wang, T., 2020. Breast cancer image classification via multi-network  
800 features and dual-network orthogonal low-rank learning. *IEEE Access*  
801 8, 27779–27792.
- 802 [62] Xu, H., Yan, J., Persson, N., Lin, W., Zha, H., 2017. Fractal dimension  
803 invariant filtering and its cnn-based implementation. In: Proceedings of  
804 the IEEE Conference on Computer Vision and Pattern Recognition. pp.  
805 3491–3499.
- 806 [63] Yamashita, R., Nishio, M., Do, R. K. G., Togashi, K., 2018. Convolu-  
807 tional neural networks: an overview and application in radiology. In-  
808 sights into Imaging, 1–19.

- 809 [64] Yu, C., Chen, H., Li, Y., Peng, Y., Li, J., Yang, F., 2019. Breast cancer  
810 classification in pathological images based on hybrid features. *Multime-*  
811 *dia Tools and Applications*, 1–21.